










Vacuum-sealed silicon photonic MEMS tunable ring resonator with an independent control over coupling and phase

PIERRE EDINGER,^{1,*}  GAEHUN JO,¹ CHRIS PHONG VAN NGUYEN,¹ ALAIN YUJI TAKABAYASHI,² CARLOS ERRANDO-HERRANZ,¹  CLEITUS ANTONY,³ GIUSEPPE TALLI,³ PETER VERHEYEN,⁴ UMAR KHAN,^{4,5}  SIMON J. BLEIKER,¹ WIM BOGAERTS,^{4,5}  NIELS QUACK,^{2,6}  FRANK NIKLAUS,¹  AND KRISTINN B. GYLFASON¹ 

¹KTH Royal Institute of Technology, Malvinas väg 10, SE-100 44 Stockholm, Sweden

²Ecole Polytechnique Fédérale de Lausanne, CM 1 364 (Centre Midi), Station 10, CH-1015 Lausanne, Switzerland

³Tyndall National Institute of Technology, Lee Maltings Complex Dyke Parade, Cork T12 R5CP, Cork, Ireland

⁴Interuniversity Microelectronics Centre, imec 1 (postbus), Kapeldreef 75, 3001 Leuven, Belgium

⁵Ghent University - IMEC, Dept. of Information Technology, Technologiepark-Zwijnaarde 126, 9052, Belgium

⁶The University of Sydney, J07 - 90 Carillon Ave, Sydney University Village, Newtown, AU 2042, Australia
*edinger@kth.se

Abstract: Ring resonators are a vital element for filters, optical delay lines, or sensors in silicon photonics. However, reconfigurable ring resonators with low-power consumption are not available in foundries today. We demonstrate an add-drop ring resonator with the independent tuning of round-trip phase and coupling using low-power microelectromechanical (MEMS) actuation. At a wavelength of 1540 nm and for a maximum voltage of 40 V, the phase shifters provide a resonance wavelength tuning of 0.15 nm, while the tunable couplers can tune the optical resonance extinction ratio at the through port from 0 to 30 dB. The optical resonance displays a passive quality factor of 29 000, which can be increased to almost 50 000 with actuation. The MEMS rings are individually vacuum-sealed on wafer scale, enabling reliable and long-term protection from the environment. We cycled the mechanical actuators for more than 4×10^9 cycles at 100 kHz, and did not observe degradation in their response curves. On mechanical resonance, we demonstrate a modulation increase of up to 15 dB, with a voltage bias of 4 V and a peak drive amplitude as low as 20 mV.

© 2023 Optica Publishing Group under the terms of the [Optica Open Access Publishing Agreement](#)

1. Introduction

Silicon photonics is emerging as a technology of choice for multiple novel computing platforms, such as artificial neural networks, microwave signal processing, and quantum computing. The ring resonator is an essential building block in silicon photonics, commonly used for filtering, sensing, and wavelength multiplexing [1]. However, active circuits require ring resonators that can be reconfigured, and current technologies in photonic foundry platforms have several limitations. For example, tunable ring resonators can be built using discrete thermo-optic phase shifters in foundries [2]. However, these consume on the order of 10 mW of static power, and thermal cross-talk prevents the independent tuning of phase and power in compact rings [3]. Carrier-depletion-based rings provide fast tuning for modulation, but the increase of propagation losses due to doping limits the quality factor [4]. Moreover, thermo-optic and carrier-depletion-based actuators are better suited for phase tuning, and tuning the coupling into

a ring relies on tunable Mach-Zehnder-Interferometers (MZIs) [5]. The MZIs are composed of discrete components and are, therefore, long and lossy.

Electrostatic microelectromechanical (MEMS) actuators have shown promise for the reconfiguration of ring resonators with low power consumption and short optical lengths [6]. However, reported devices do not offer tuning over both phase and power, have relatively low quality factors, or are not compatible with photonic foundry processes. Lee et al. reported an add-drop disk resonator with MEMS-based variable coupling ratio as early as 2005 on a 1.2 μm thick Silicon-on-Insulator (SOI) substrate, but with a low quality factor and limited tuning [7]. The same group also demonstrated an add-drop microtoroidal resonator with a Free Spectral Range (FSR) of 5.2 nm and a MEMS-tunable quality factor of up to 110k [8]. However, this approach required a high-temperature hydrogen annealing step to form the toroid rim and the bonding of a second device layer for the vertically movable bus waveguides. Multiple MEMS-tunable ring resonators have also been shown on single-layer SOI wafers with a 220 nm thin device layer. Takahashi et al. demonstrated a ring resonator attached to a comb-drive actuator that can be moved away from two fixed bus waveguides for extinction ratio tuning, with an FSR of 8.45 nm but a low maximum quality factor of 3200 [9]. Sattari et al. demonstrated a similar filter configuration but with out-of-plane displacement of the entire ring, with an FSR of 5.1 nm and a quality factor of 1557 [10]. Ikeda et al. reported an all-pass ring resonator with a tunable round-trip physical length, providing resonance tuning up to 26 nm, but with a maximum quality factor of 4000 [11,12]. Errando-Herranz et al. demonstrated all-pass ring resonators with an out-of-plane actuator for resonance tuning, which provided quality factors up to 12k, but a smaller FSR of 5 nm and resonance tuning of 0.3 nm [13,14]. Park et al. presented fully reconfigurable add-drop ring resonators using out-of-plane actuators that can be cascaded into a 1D coupled resonator optical waveguide (CROW). However, the FSR was limited to 0.124 nm due to a long round-trip length [15]. Finally, none of the published ring resonators included a sealing step for protection, which is critical for the long-term reliability of MEMS actuators [16].

Here, we report an add-drop ring resonator, where the input coupling, output coupling, and round-trip phase can all be independently tuned using MEMS comb-drive actuators. The coupling is controlled by physically changing the gap between the bus and ring waveguides, while the round-trip phase is tuned by perturbing the modal cross-section of the ring waveguide. Our device was implemented on a silicon photonics foundry platform (IMEC's iSiPP50G) and sealed in a vacuum cavity using wafer-level sealing. Due to its foundry compatibility, low power consumption, long FSR, and high optical quality factor, this ring is an excellent candidate to be used as a building block in programmable silicon photonic circuits.

2. MEMS ring resonator design

The tunable MEMS ring resonator comprises a circular single-side-suspended rib waveguide optical cavity, two MEMS actuators for phase shifting inside the ring, and MEMS-movable bus waveguides to control the input and output coupling to the ring; see Fig. 1. The bus waveguides are anchored to the edge of a MEMS cavity, which is defined by locally etching back the Back-End-Of-Line (BEOL) dielectric stack. Optical and electrical transitions connect the MEMS device to standard oxide-clad components outside the MEMS cavity. The detailed dimensions of the actuators and waveguides are included in [Supplement 1 Fig. S1](#).

2.1. Ring waveguide

Electrostatic photonic MEMS actuators rely on suspended and movable waveguide sections to change the modal cross-section of the guided light. As a result, mechanical anchors are required to support the suspended waveguides, which can increase optical loss. We designed the ring resonator waveguide as a continuous single-side-suspended rib waveguide to minimize the round-trip loss typically introduced by discrete anchors. As illustrated in Fig. 2, the ring

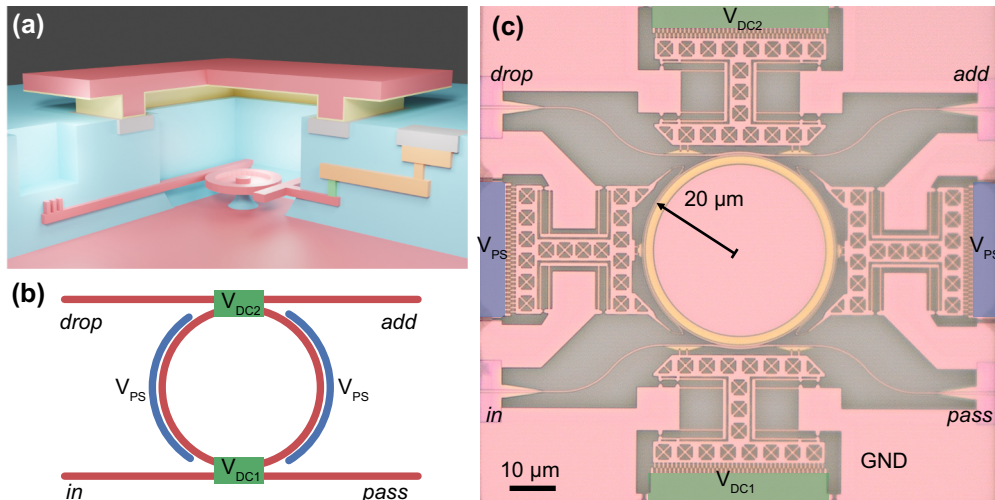


Fig. 1. Vacuum-sealed ring resonators for silicon photonics. (a) 3D sketch of our ring resonator composed of suspended waveguides and MEMS actuators, sealed using 25 μm thin silicon caps. (b) Microscope view of our fabricated device using comb-drive MEMS actuators to tune input coupling, output coupling, and round-trip phase independently.

waveguide is anchored by a 70 nm thin disk membrane supported on a central pillar. This uniform anchor provides transition-free mechanical support while the ring waveguide maintains its single-mode condition. The ring waveguide width is 400 nm, chosen as a trade-off between achievable phase shift and losses. Larger waveguide widths would reduce the propagation losses due to sidewall scattering by increasing the mode confinement. However, the effective index tuning range is larger when the mode is less confined. The ring has a radius of 20 μm to obtain a relatively short round-trip length while providing a sufficient area to place the phase-shifting actuators. When unloaded, the ring has a simulated FSR of 4.2 nm at 1550 nm.

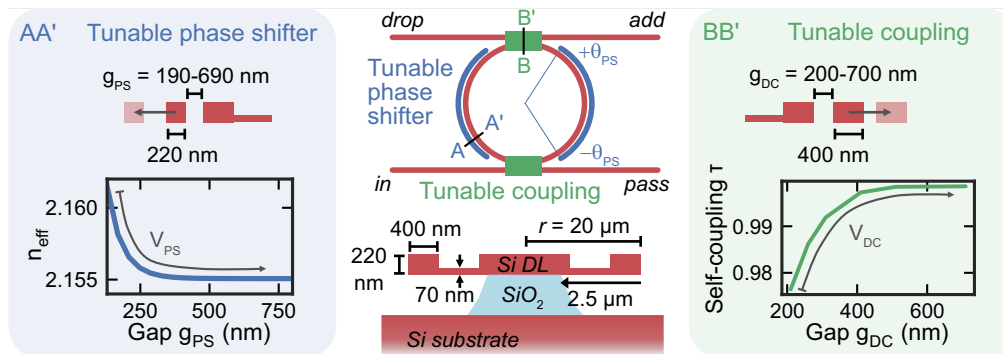


Fig. 2. Add-drop ring resonator design. A circular single-side rib waveguide is mechanically supported using a disk membrane with a 2.5 μm undercut. Two MEMS actuators with common bias tune the effective index of the ring waveguide along 55% of the ring length for resonance tuning. Two additional MEMS actuators control the coupling between ring waveguide and bus waveguides for extinction ratio tuning.

2.2. Phase shifters

The MEMS phase shifters are based on our previously published design [17], with a reduced footprint and curved tuning ribs to follow the ring waveguide curvature. The MEMS actuators were chosen for their low power consumption (1 nW for π -modulation at 1 kHz, and 1 μ W for π -modulation at 400 kHz), their large linear phase shifting range and their actuation speed.

A phase shift is accumulated along the interaction regions between the ring waveguide and the evanescent field perturbing silicon beam, which can be calculated by integrating the differential change in the effective index along the ring curvature, according to

$$\Delta\phi(\lambda, V_{PS}) = \frac{2\pi}{\lambda} \int_{-\theta_{PS}}^{\theta_{PS}} \delta n_{\text{eff}}(\theta, \lambda, V_{PS}) r d\theta, \quad (1)$$

with $\Delta\phi(\lambda, V_{PS})$ the phase shift, λ the wavelength, V_{PS} the phase shifter actuation voltage, θ_{PS} half the angle over which the phase shifting perturber interacts with the ring waveguide, r the disk radius, and $\delta n_{\text{eff}}(\theta, \lambda, V_{PS})$ the wavelength and voltage-dependent change of effective index n_{eff} along the interaction region. Now the effective index change is

$$\delta n_{\text{eff}}(\theta, \lambda, V_{PS}) = n_{\text{eff}}(\lambda, g(\theta, V_{PS})) - n_{\text{eff},0}(\lambda), \quad (2)$$

with $g(\theta, V_{PS})$ the actuation and angle dependent gap, and $n_{\text{eff},0}(\lambda)$ the effective index of the waveguide in the passive state of the device. When using a MEMS comb drive actuator, the voltage-dependent gap along the ring waveguide can be expressed as

$$g(\theta, V_{PS}) \approx g_0 + \frac{1}{k} \epsilon N_F \frac{t}{g_{CD}} V_{PS}^2 \cos(\theta), \quad (3)$$

with g_0 the initial gap, k the stiffness of the actuator along the displacement axis, ϵ the permittivity of the dielectric in the gap, N_F the number of comb-drive fingers, t the device layer thickness, and g_{CD} the finger gap. The second term is the displacement and is based on a simple comb-drive actuator model, which does not include any fringing fields [18]. The maximum displacement is limited to 500 nm using mechanical stoppers. This limit is mainly set to avoid finger collapse due to the parasitic capacitance at the fingertips resulting in instability after large displacements.

For the 20 μ m radius add-drop ring, the interaction angle $2\theta_{PS}$ is 100 degrees, corresponding to an interaction length of 35 μ m per phase shifter. The initial gap g_0 is 190 nm, and the waveguide width is 400 nm. At a wavelength of 1550 nm, the simulated maximum total phase shift is 0.2π , corresponding to an expected resonance shift of 0.4 nm. The actuators used for the phase shifters have a stiffness k of 1.9 N/m and a shuttle mass of 147 fg.

2.3. Tunable couplers

The tunable couplers rely on the same type of comb-drive actuator and shuttle as the phase shifters. Two side anchors attach the movable bus waveguide to the shuttle and ensure uniform gap change throughout the directional coupler. The movable bus waveguide is also anchored to the silicon edge of the MEMS cavity, directly connected to standard waveguides using oxide-to air-clad transitions. The waveguide portions connecting the edge anchors to the directional couplers are S-shaped to avoid buckling due to the relaxation of compressive strain in the device layer upon release. The directional couplers are slightly asymmetric since the ring waveguide is a single-side rib waveguide, while the movable bus is a strip waveguide. The simulated change in the self-coupling coefficient to the horizontal coupling gap is plotted in Fig. 2 (Lumerical 3D FDTD). In its passive state, the coupling gap is 200 nm, resulting in a self-coupling coefficient of 0.976 at 1550 nm. As the coupling gap is increased, the self-coupling increases, up to the simulated value of 0.999 for a gap of 700 nm, corresponding to the maximum displacement

allowed by the mechanical stoppers of the comb-drive actuators. The actuators used for the two tunable couplers are stiffer, with $k = 3.7$ N/m, due to the bus waveguide, and have a shuttle mass of 165 fg.

3. Device fabrication

We implemented our MEMS ring resonators on IMEC iSiPP50G silicon photonics foundry wafers that were post-processed to release the MEMS and then packaged. The post-processing was done on 100 mm sub-wafers that were cut out of the 200 mm diameter foundry wafers [19]. A sketch of the final cross-section of the sealed ring is shown in Fig. 3(a). Only a few post-processing steps are required to remove the Buried-Oxide layer (BOx) underneath the movable and suspended parts and thus release them. The removal of the BOx layer is limited to cavities surrounding the MEMS devices, and all other features of the iSiPP50G platform remain unaffected. In particular, the MEMS actuators benefit from the available selective doping of the Si device layer and two-layer metal routing, providing a flexible and low-resistance electrical path. A microscope top view of the ring resonator before sealing is shown in Fig. 3(b).

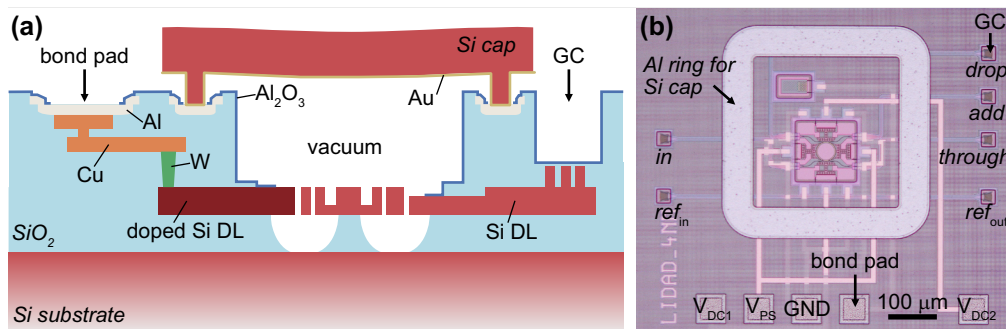


Fig. 3. Ring fabrication. (a) Cross-section sketch of our sealed photonic MEMS device. The ring was designed on IMEC's iSiPP50G platform, released using an alumina masking layer and vHF etching, and sealed using Au-to-Al thermo-compression bonding. (b) Microscope top view of a ring resonator before sealing.

Finally, we sealed the ring resonators in vacuum by bonding thin silicon caps onto the photonic device layer, using our previously published wafer-bonding approach [20]. To seal the wafers, we first fabricated 25 μm thin silicon sealing caps on a separate 100 mm diameter SOI wafer. We patterned a 9 μm wide protruding ring in the cap to encircle and seal individual MEMS cavities during the bonding step. We covered the sealing caps with a 2 μm thick gold layer. We performed thermo-compression bonding between the iSiPP50G aluminum layer and the gold layer on the caps in vacuum using a commercial wafer bonder (EVG520 IS 200mm Wafer Bonding System, EV Group, Austria). Finally, we removed the handle layer of the SOI sealing cap wafer by deep reactive ion etching (STS ICP DRIE) to gain access to bond pads and grating couplers.

4. Device characterization

We characterized the transmission of our MEMS ring resonator in the wavelength range from 1500 to 1580 nm. The passive spectra are plotted in Fig. 4(a). As illustrated in Fig. 3(b), the circuit includes a reference waveguide that passes under the sealing lid but not through the MEMS cavity. This reference allows us to separate the wavelength dependence and loss of the grating couplers from that of the ring and the MEMS cavity. As plotted in Fig. 4(a), the envelope of the transmission from input to through port follows the transmission through the 450 nm oxide-clad reference strip waveguide within 0.5 dB, suggesting that the ring insertion loss is low. A more

precise insertion loss measurement would require dedicated test structures. The FSR increases linearly by 10% over the range of the tunable laser, as shown in Fig. 4(b). We successively measured the transmission at the *through*, *drop*, and *add* ports by moving the output fiber. The off-resonance extinction between *through* and *drop* is larger than 30 dB over the measured range and larger still between *through* and *add*. However, a decrease in the resonances' extinction ratios can be observed at longer wavelengths; see Fig. 4(c). Additionally, resonances can clearly be observed in the *add* port. Both are due to coupling between the clockwise and counter-clockwise propagating modes in the ring, leading to resonance splitting and power coming out of the *add* port [21].

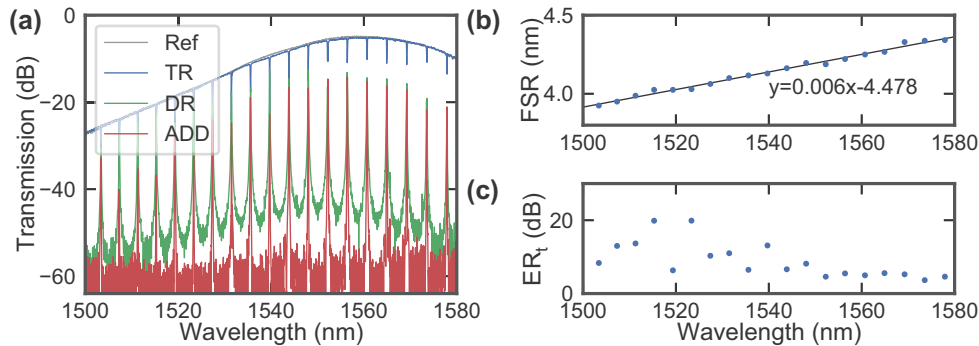


Fig. 4. Passive characterization of the sealed add-drop ring resonator. (a) Passive transmission from 1500 to 1580 nm. (b) Corresponding FSR with respect to wavelength. (c) Extinction ratios of the resonances at the *through* (TR) port.

4.1. Static characterization

We verified that the different actuators provide the intended response by tracking the transmission spectra with respect to each actuation bias. We repeated the transmission measurements from 1500 to 1580 nm for both *through* and *add* ports, and each actuation bias (V_{DC1} , V_{PS} , V_{DC2}). In Fig. 5, we present the normalized transmission for the resonance at 1539.7 nm and for each actuation bias. V_{DC1} and V_{DC2} mainly control the extinction ratios of the resonances and the maximum power at the *drop* port. However, both tunable couplers also induce a resonance shift. V_{PS} only induces a shift in resonance. The *through* (TR) and *drop* (DR) measurements were not done simultaneously, and we attribute the offsets in the passive state to slow resonance shifts due to temperature drifts. We extracted the extinction ratios at the *through* port and the phase shift versus wavelength for all resonances from 1500 to 1580 nm. We did not observe any hysteresis in the response for actuation voltages up to 40 V. However, some hysteresis could be observed when monitoring the transmission at the *drop* port and increasing the V_{DC1} bias up to 50 V; see Supplement 1 Fig. S5. This hysteresis suggests that the actuators used in the couplers reach the stoppers at actuation voltages between 40 V and 45 V, and initially stick to it as the bias is lowered again. The actuators used in the phase shifters are expected to reach the stoppers at a lower voltage, as the total spring constant is lower while the stopper gap is the same. However, no hysteresis could be observed, likely due to the diminishing phase shift response for actuation voltages above 30 V; see Fig. 2.

We extracted the quality factor of the ring at 1539.7 nm by fitting the spectra at the *drop* port; see Fig. 5(d). The fitting was done using an ideal transmission model that includes the self-coupling coefficients and the round-trip attenuation as free parameters [1]. The phase shifters do not affect the quality factor significantly, suggesting that they have a low variable loss. The quality factor increases when the directional couplers are actuated, which is expected

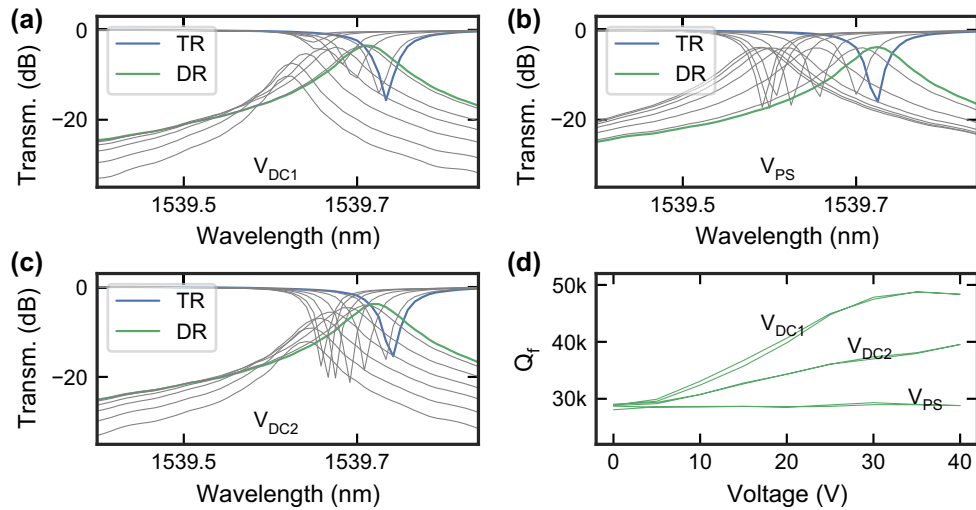


Fig. 5. (a)-(c) DC actuation up to 40 V of the three actuators V_{DC1} , V_{PS} , and V_{DC2} , respectively, in the wavelength region around the resonance at 1539.7 nm. The transmission is normalized to the reference waveguide measurement. (d) Extracted quality factor versus voltage for all three actuators.

since the actuators reduce the coupling to the bus waveguides, lowering the overall ring losses. However, the couplers are identical and should result in the same increase in quality factor with actuation, since the quality factor of add-drop ring resonators depends on the coupling coefficients symmetrically [1]. The difference in quality factor tuning could be explained by a slight asymmetry between both components or by the presence of optical reflections in the ring. The model does not consider the counter-clockwise propagating mode that can be excited by back-reflections [21]. At longer wavelengths, we observed pronounced peak-splitting for which the ideal model can no longer be used; see [Supplement 1 Fig. S4](#).

The different actuators can also be used simultaneously. For instance, the phase shifters can be used to compensate for the parasitic resonance shift of the couplers. We demonstrate this compensation by measuring the transmission at the *through* port from 1539 to 1540 nm. The resonance extinction ratio can be tuned from 0 to 30 dB using both V_{DC1} and V_{DC2} ; see [Fig. 6\(a\)](#). However, both couplers also induce symmetric phase shifts; see [Fig. 6\(b\)](#). We used the two-dimensional map of the resonance shift to set a compensation bias on the phase shifters, using linear interpolation; see [Supplement 1 Fig. S6](#). When remeasuring the device response from 1539 to 1540 nm with respect to V_{DC1} and V_{DC2} , but adding the compensating V_{PS} offsets, we obtain a very similar extinction ratio map ([Fig. 6\(d\)](#)), but with a significantly reduced wavelength shift; see [Fig. 6\(e\)](#).

4.2. Dynamic characterization

We also investigated the frequency response of the MEMS actuators. We used a lock-in amplifier (HF2LI, Zurich Instruments) to successively drive V_{DC1} , V_{PS} and V_{DC2} and measure the power modulation at the *through* port from 100 kHz to 1.6 MHz. All AC measurements were done with a laser power of 4 mW. For each actuator, we first set the wavelength to the -3 dB point (blue detuning) on the slope of the resonance at 1539.7 nm. The wavelength of the -3 dB point depends on the DC offset, and we repeated the measurement for offsets of 4 and 8 V. In [Fig. 7](#), we compare the responses of all three actuators for DC offsets of 4 V and AC peak amplitudes of 100 mV. The phase shifter exhibits a main resonance at 554 kHz, corresponding to the fundamental

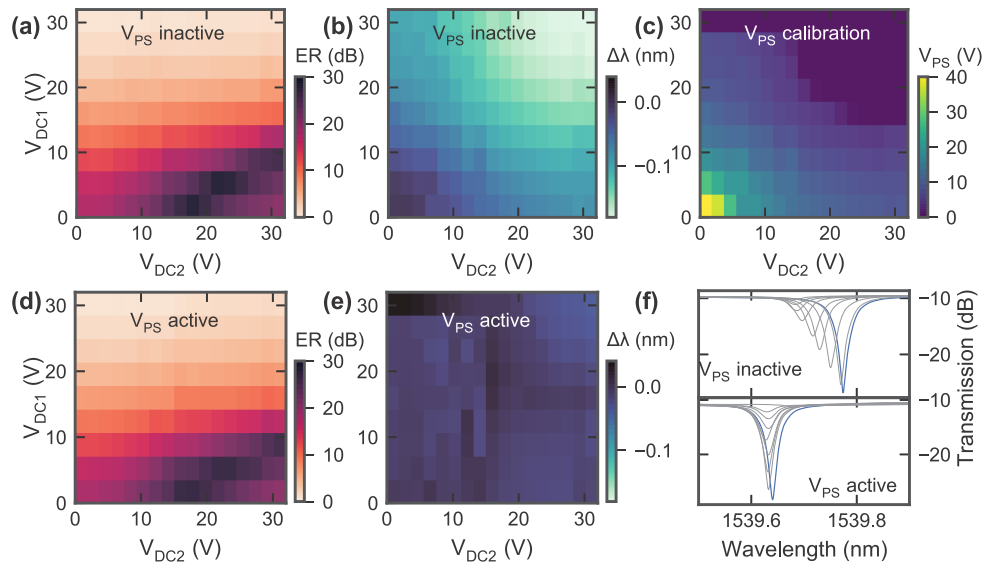


Fig. 6. Simultaneous tuning of the resonance at 1539.7 nm using V_{DC1} , V_{PS} , and V_{DC2} . (a) Two-dimensional actuation map (V_{DC1} , V_{DC2}) with $V_{PS} = 0$ V of the extinction ratio, and (b) of the resonance shift. (c) V_{PS} offset map for (d) extinction ratio tuning (e) without wavelength shift. (f) Example of extinction ratio tuning with and without the V_{PS} offsets.

in-plane eigenmode of the actuator. For the two directional couplers, the main resonance is around 719 kHz, again corresponding to the fundamental in-plane eigenmode. Both frequencies agree well with the simulated values of 551 and 756 kHz, respectively; see [Supplement 1](#) Figs. S2-3. However, multiple additional resonances can be observed within the measured frequency range. Those can be attributed to out-of-plane eigenmodes of the shuttle (lower frequencies) and sub-structures (higher frequencies). In an ideal actuator, out-of-plane resonances should not be excited using the MEMS actuators. However, a small vertical offset between fixed and suspended comb-drive electrodes could add an out-of-plane component to the electrostatic force, leading to the excitation of some out-of-plane resonances. In particular, the resonances between 200 and 350 kHz depend on the DC offset: when increased to 8 V, the second resonance is suppressed; see [Supplement 1](#) Fig. S7.

However, not all resonances can be explained by electro-mechanical excitation via the electrostatic actuator. In particular, an excitation on the phase shifter bias results in resonances at 719 and 857 kHz, which do not match any of the simulated phase shifter mechanical eigenmodes. Those two resonances could originate from optomechanical coupling to the couplers [22,23]. As the power in the ring is modulated by tuning in and out of optical resonance, the mechanical resonances of the non-driven actuators could be excited through a change in the optical gradient force across the directional couplers.

We extracted the mechanical quality factor of the main resonances with DC offsets of 4 and 8 V. We obtained a mechanical quality factor above 100 for the couplers and up to 70 for the phase shifters; see [Supplement 1](#) Table S1. The values are an order of magnitude higher than for our previously published phase shifters in ambient air [20]. However, the actuators were not designed for their mechanical resonant properties, and higher mechanical quality factors can be achieved with dedicated mechanical anchors [24].

We evaluated the long-term reliability of the device by driving the MEMS actuators at a frequency of 100 kHz for a duration of 12 hours, corresponding to over 4×10^9 cycles. We did

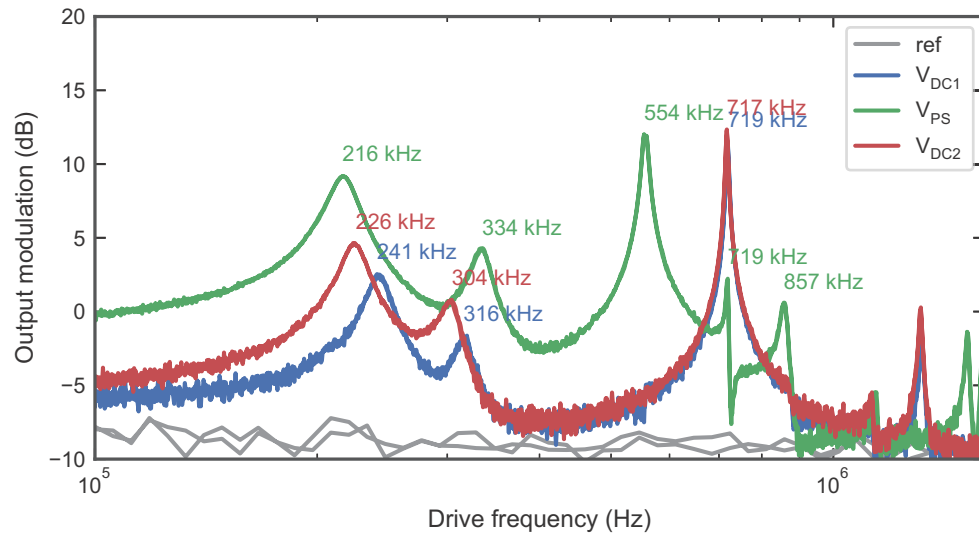


Fig. 7. Frequency response of the sealed add-drop ring resonator. All measurements were done with a DC offset of 4 V and a peak drive amplitude of 100 mV.

not observe any significant change in the response curves of the three actuators after the cycling; see [Supplement 1 Fig. S9](#). For the tests, we set the DC offset of the actuators to 5 V, and the AC peak drive amplitude to 1 V.

5. Discussion

Our ring resonators are the first sealed MEMS-tunable rings implemented in a silicon photonic foundry. Compared to other single-layer MEMS ring resonators, our rings display the highest quality factor and the most degrees of control; see [Table 1](#). Only Park et al. previously demonstrated independent tuning of phase and power in add-drop ring resonators, but the long discrete active elements led to a very short FSR of 0.124 nm [[15](#)]. Moreover, our ring resonators show the highest degree of integration towards the foundry fabrication of silicon photonic circuits and long-term reliability with dedicated MEMS sealing caps. Our rings were designed and fabricated on 200 mm diameter silicon photonic wafers (IMEC's iSiPP50G platform). The post-processing steps to release the MEMS actuators, and the subsequent wafer-level sealing of the MEMS cavities, were performed on cored 100 mm silicon wafers. The demonstrated foundry integration enabled multi-layer electrical routing, critical for circuits, and selective device layer doping, enabling operation up to the mechanical cut-off frequency instead of being limited by electrical RC cut-off as in previous silicon photonic MEMS without actuator doping [[25](#)]. Additionally, we did not measure any cross-talk between the actuators during the static characterization. A ring resonator comprising multiple independent thermal actuators within a similarly small footprint would be significantly influenced by thermal crosstalk [[3](#)].

On the other hand, our ring resonators are limited in the wavelength tuning range, and the higher quality factor led to peak-splitting, which lowered the achieved extinction ratios at longer wavelengths. The wavelength tuning range could be increased by reducing the gap between the ring waveguide and the effective index perturber instead of increasing it. This can be implemented with minimal adjustments to the actuators, which we have reported in the context of a nonvolatile phase switch [[26](#)]. The peak-splitting, associated with reflections within the round-trip, could possibly be compensated for using a tunable reflector [[27](#)]. A dedicated MEMS-based actuator

Table 1. Performance comparison of silicon photonic MEMS ring resonators.

Platform	Sealed	Type ^a	Control	FSR (nm)	Q	$\Delta\lambda$ (nm)	V (V)	ER _t (dB)	Ref.
iSiPP50G ^b	Yes	AD	PS+2DC	4.2	>25k	0.15	40	30	Here
iSiPP50G ^b	No	AD	DC	5.1	1.6k	-	27	25	[10]
SOI	No	AD	DC	8.45	3.2k	-	29	-	[9]
SOI	No	AP	PS	3.3	4k	10	25	10	[11]
SOI	No	AP	PS	21	1.7k	27	25	8	[12]
SOI	No	AD	PS	1.2	10k	0.53	-	7	[28]
SOI	No	AD	PS+2DC	0.124	-	0.13	10	14	[15]

^aRing type is either Add-Drop (AD) or All-Pass (AP).

^bImplemented on IMEC's iSiPP50G, post-processed on 100 mm wafers.

could be added to one edge of the ring, although this would reduce the available interaction length for phase-shifting.

To our knowledge, this is the first time that on-chip vacuum-sealed ring resonators were shown. While our rings were not designed for optomechanics, our platform could be well suited for such experiments [23,29] without requiring a vacuum chamber. However, the lack of air damping also complicates the use of the ring at frequencies above 200 kHz due to the presence of multiple mechanical resonances. We did not observe any damage with peak driving amplitudes up to 200 mV, but larger AC drives could lead to the irreversible collapse of the actuators to the substrate due to the amplified displacement. For programmable circuits, resonance-free operation up to the -3 dB cut-off could be preferred. An option could be to seal a gas with increased damping instead of sealing the ring in vacuum. Alternatively, the actuators could be optimized for resonance-free operation up to the MHz range by increasing their stiffness and reducing their mass.

6. Conclusion

We have demonstrated ring resonators with independent MEMS tuning of coupling and round-trip phase on a silicon photonics platform. The rings are individually vacuum-sealed using wafer-scale thermo-compression bonding. The sealing protects the MEMS during the following packaging steps and ensures reliable operation over time. Our demonstration of sealed MEMS tunable ring resonators fills a missing gap in active photonic circuits. The rings have a low power consumption that thermal actuators cannot offer, while the protective sealing enables subsequent packaging and, therefore, reliable real-life use of photonic MEMS technology. Moreover, the availability of on-chip vacuum-sealed ring resonators is expected to greatly benefit the field of optomechanics.

Funding. This work has received funding from the European Union's Horizon 2020 research and innovation programme under grant agreements No. 780283 (MORPHIC), and No. 825272 (ULISSES).

Acknowledgments. We thank Dr. Max Yan for access to measurement equipment, Mikael Bergqvist for assistance with measurement setups, and the EV Group (St. Florian am Inn, Austria) for the help with the wafer-bonding experiments. Parts of this work were presented at CLEO 2022, paper SF4M.5 [30]. The work reported in this manuscript was performed while N. Quack was at EPFL (affiliation 2), and the manuscript was composed while N. Quack was at the University of Sydney (affiliation 6).

Disclosures. The authors declare no conflicts of interest.

Data availability. Data underlying the results presented in this paper are not publicly available at this time but may be obtained from the authors upon reasonable request.

Supplemental document. See [Supplement 1](#) for supporting content.

References

1. W. Bogaerts, P. De Heyn, T. Van Vaerenbergh, K. De Vos, S. Kumar Selvaraja, T. Claes, P. Dumon, P. Bienstman, D. Van Thourhout, and R. Baets, "Silicon microring resonators," *Laser & Photonics Reviews* **6**(1), 47–73 (2012).
2. D. Pérez, I. Gasulla, L. Crudgington, D. J. Thomson, A. Z. Khokhar, K. Li, W. Cao, G. Z. Mashanovich, and J. Capmany, "Multipurpose silicon photonics signal processor core," *Nat. Commun.* **8**(1), 636 (2017).
3. M. Milanizadeh, D. Aguiar, A. Melloni, and F. Morichetti, "Canceling Thermal Cross-Talk Effects in Photonic Integrated Circuits," *J. Lightwave Technol.* **37**(4), 1325–1332 (2019).
4. Q. Xu, B. Schmidt, S. Pradhan, and M. Lipson, "Micrometre-scale silicon electro-optic modulator," *Nature* **435**(7040), 325–327 (2005).
5. L. Chen, N. Sherwood-Droz, and M. Lipson, "Compact bandwidth-tunable microring resonators," *Opt. Lett.* **32**(22), 3361–3363 (2007).
6. C. Errando-Herranz, A. Y. Takabayashi, P. Edinger, H. Sattari, K. B. Gylfason, and N. Quack, "MEMS for Photonic Integrated Circuits," *IEEE J. Sel. Top. Quantum Electron.* **26**(2), 1–16 (2020).
7. M.-C. Lee and M. Wu, "MEMS-actuated microdisk resonators with variable power coupling ratios," *IEEE Photonics Technol. Lett.* **17**(5), 1034–1036 (2005).
8. J. Yao, D. Leuener, M.-C. M. Lee, and M. C. Wu, "Silicon Microtoroidal Resonators With Integrated MEMS Tunable Coupler," *IEEE J. Sel. Top. Quantum Electron.* **13**(2), 202–208 (2007).
9. K. Takahashi, Y. Kanamori, Y. Kokubun, and K. Hane, "A wavelength-selective add-drop switch using silicon microring resonator with a submicron-comb electrostatic actuator," *Opt. Express* **16**(19), 14421–14428 (2008).
10. H. Sattari, A. Y. Takabayashi, P. Edinger, P. Verheyen, K. B. Gylfason, W. Bogaerts, and N. Quack, "Silicon photonic microelectromechanical systems add-drop ring resonator in a foundry process," *Journal of Optical Microsystems* **2**(04), 044001 (2022).
11. T. Ikeda and K. Hane, "A microelectromechanically tunable microring resonator composed of freestanding silicon photonic waveguide couplers," *Appl. Phys. Lett.* **102**(22), 221113 (2013).
12. H. M. Chu and K. Hane, "A Wide-Tuning Silicon Ring-Resonator Composed of Coupled Freestanding Waveguides," *Photonics Technology Letters, IEEE* **26**(14), 1411–1413 (2014).
13. C. Errando-Herranz, F. Niklaus, G. Stemme, and K. B. Gylfason, "A MEMS tunable photonic ring resonator with small footprint and large free spectral range," in *Solid-State Sensors, Actuators and Microsystems (TRANSDUCERS), 2015 Transducers-2015 18th International Conference on*, (IEEE, 2015), pp. 1001–1004.
14. C. Errando-Herranz, F. Niklaus, G. Stemme, and K. B. Gylfason, "Low-power microelectromechanically tunable silicon photonic ring resonator add-drop filter," *Opt. Lett.* **40**(15), 3556–3559 (2015).
15. Y. J. Park, D. U. Kim, D. Y. Kim, M. S. Hong, A. Y. Takabayashi, Y. Jeong, J. Park, S. Han, N. Quack, K. Yu, and S. Han, "Fully Reconfigurable Coupled-Resonator Optical Waveguides (CROWs) with 10 nW Static Power MEMS," in *Conference on Lasers and Electro-Optics (2021)*, paper STh1Q.5, (Optical Society of America, 2021), p. STh1Q.5.
16. W. M. Van Spengen, R. Modlinski, R. Puers, and A. Jourdain, "Failure Mechanisms in MEMS/NEMS Devices," in *Springer Handbook of Nanotechnology*, B. Bhushan, ed. (Springer, 2017), pp. 1437–1457.
17. P. Edinger, A. Y. Takabayashi, C. Errando-Herranz, U. Khan, H. Sattari, P. Verheyen, W. Bogaerts, N. Quack, and K. B. Gylfason, "Silicon photonic microelectromechanical phase shifters for scalable programmable photonics," *Opt. Lett.* **46**(22), 5671–5674 (2021).
18. R. Legtenberg, A. W. Groeneveld, and M. Elwenspoek, "Comb-drive actuators for large displacements," *J. Micromech. Microeng.* **6**(3), 320–329 (1996).
19. W. Bogaerts, A. Y. Takabayashi, P. Edinger, G. Jo, I. Zand, P. Verheyen, M. Jezzini, H. Sattari, G. Talli, and C. Antony, "Programmable silicon photonic circuits powered by MEMS," in *Smart Photonic and Optoelectronic Integrated Circuits 2022*, vol. 12005 (SPIE, 2022), pp. 55–69.
20. G. Jo, P. Edinger, S. J. Bleiker, X. Wang, A. Y. Takabayashi, H. Sattari, N. Quack, M. Jezzini, J. S. Lee, P. Verheyen, I. Zand, U. Khan, W. Bogaerts, G. Stemme, K. B. Gylfason, K. B. Gylfason, F. Niklaus, and F. Niklaus, "Wafer-level hermetically sealed silicon photonic MEMS," *Photonics Res.* **10**(2), A14–A21 (2022).
21. A. Li, T. Van Vaerenbergh, P. De Heyn, P. Bienstman, and W. Bogaerts, "Backscattering in silicon microring resonators: a quantitative analysis," *Laser & Photonics Reviews* **10**(3), 420–431 (2016).
22. J. Roels, I. De Vlamincq, L. Lagae, B. Maes, D. Van Thourhout, and R. Baets, "Tunable optical forces between nanophotonic waveguides," *Nat. Nanotechnol.* **4**(8), 510–513 (2009).
23. B. Dong, H. Cai, G. I. Ng, P. Kropelnicki, J. M. Tsai, A. B. Randles, M. Tang, Y. D. Gu, Z. G. Suo, and A. Q. Liu, "A nanoelectromechanical systems actuator driven and controlled by Q-factor attenuation of ring resonator," *Appl. Phys. Lett.* **103**(18), 181105 (2013).
24. J. Chan, A. H. Safavi-Naeini, J. T. Hill, S. Meenehan, and O. Painter, "Optimized optomechanical crystal cavity with acoustic radiation shield," *Appl. Phys. Lett.* **101**(8), 081115 (2012).
25. T. Nagai and K. Hane, "Silicon photonic microelectromechanical switch using lateral adiabatic waveguide couplers," *Opt. Express* **26**(26), 33906–33917 (2018).
26. P. Edinger, A. Y. Takabayashi, C. Errando-Herranz, U. Khan, C. Antony, G. Talli, P. Verheyen, W. Bogaerts, N. Quack, and K. B. Gylfason, "A Bistable Silicon Photonic Mems Phase Switch For Nonvolatile Photonic Circuits," in *2022 IEEE 35th International Conference on Micro Electro Mechanical Systems Conference (MEMS)*, (2022), pp. 995–997.
27. A. Li and W. Bogaerts, "Fundamental suppression of backscattering in silicon microrings," *Opt. Express* **25**(3), 2092–2099 (2017).
28. C. Errando-Herranz, F. Niklaus, G. Stemme, and K. B. Gylfason, "A Low-power MEMS Tunable Photonic Ring Resonator for Reconfigurable Optical Networks," in *The 28th IEEE International Conference on Micro Electro Mechanical Systems (MEMS), Jan 2015*, (2015).

29. B. Dong, H. Cai, L. K. Chin, J. G. Huang, Z. C. Yang, Y. D. Gu, G. I. Ng, W. Ser, D. L. Kwong, and A. Q. Liu, "A silicon-nanowire memory driven by optical gradient force induced bistability," *Appl. Phys. Lett.* **107**(26), 261111 (2015).
30. P. Edinger, C. P. V. Nguyen, A. Y. Takabayashi, C. Antony, G. Talli, P. Verheyen, U. Khan, W. Bogaerts, N. Quack, and K. B. Gylfason, "Add-drop silicon ring resonator with low-power MEMS tuning of phase and coupling," in *Conference on Lasers and Electro-Optics (2022), paper SF4M.5*, (Optica Publishing Group, 2022), p. SF4M.5.